Observation of the Antimatter Hypernucleus ${}^{4}_{\bar{\Lambda}}\overline{\mathrm{H}}$

The STAR Collaboration∗

Antimatter is a research topic of fundamental interest. Sufficient matter-antimatter asymmetry in the early Universe created the matter-dominated world today. The origin of this asymmetry is not completely understood to date. High-energy nuclear collisions create conditions similar to the Universe microseconds after the Big Bang, with comparable amounts of matter and antimatter [1–6]. Much of the antimatter created escapes the rapidly expanding fireball without annihilation, making such collisions an effective experimental tool to create heavy antimatter nuclear objects and study their properties [7–15]. In this paper, we report the first observation of the antimatter hypernucleus ${}^{4}_{\bar{\Lambda}}\overline{\mathrm{H}}$, composed of an $\bar{\Lambda}$, an antiproton and two antineutrons. The discovery was made through its two-body decay after production in ultrarelativistic heavy-ion collisions by the STAR experiment at the Relativistic Heavy Ion Collider [16,17]. In total, 15.6 candidate ${}^{4}_{\bar{\Lambda}}\overline{\mathrm{H}}$ antimatter hypernuclei are obtained with an estimated background count of 6.4. Lifetimes of the antihypernuclei ${}^{3}_{\bar{\Lambda}}\overline{\mathrm{H}}$ and ${}^{4}_{\bar{\Lambda}}\overline{\mathrm{H}}$ are measured and compared with the lifetimes of their corresponding hypernuclei, testing the symmetry between matter and antimatter. Various production yield ratios among (anti)hypernuclei and (anti)nuclei are also measured and compared with theoretical model predictions, shedding light on their production mechanism.

In 1928, Paul Dirac found possible solutions with positive and negative energies to his eponymous equation that describes the relativistic quantum behavior of the electron [18]. It was realized in the following years that the negative-energy solution actually indicates a new particle with the same

mass as an electron, but the opposite charge [19]. This new particle was discovered by Carl Anderson in cosmic rays in 1932 [20] and named the positron. This established the theoretical framework and the experimental foundation for the study of antimatter. With the advancement of detectors and accelerators, many more antimatter particles have been discovered. Figure 1 illustrates the masses vs. discovery years of a series of antimatter particles [7,8,20–27]. Among them, ${}^{4}_{\bar{\Lambda}}\overline{\mathrm{H}}$, whose discovery is described in this paper, is the heaviest antimatter nuclear and hypernuclear cluster observed to date.

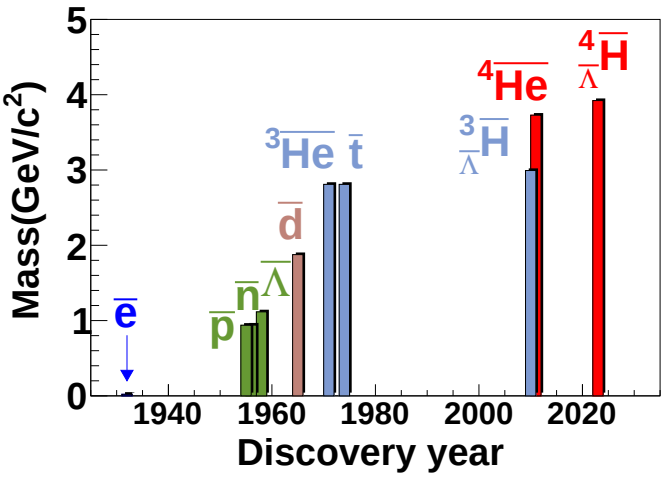

Figure 1: Masses vs. discovery years of selected antimatter particles, including the positron, antinucleons, $\overline{\Lambda}$ and antimatter (hyper)nuclear clusters.

Antimatter readily annihilates with matter, making it difficult to observe antimatter nuclear clusters in the Universe. However relativistic heavy-ion collisions can create the quark-gluon-plasma state that existed in the first few microseconds of the Universe after the Big Bang, with nearly equal amounts of matter and antimatter [1–6]. The collision system expands and cools rapidly, allowing some antimatter to decouple from matter. This makes heavy-ion collisions an effective

tool to create and study antimatter nuclei or hypernuclei [9–15].

The strange quark is the third lightest of all six flavors of quarks. It decays via the weak interaction, making it much rarer in nature than the lighter up and down quarks, which constitute nucleons in atomic nuclei. A hyperon (e.g Λ) is a baryon containing at least one strange quark. A hypernucleus is a bound state of hyperons and nucleons. In this paper, the Solenoidal Tracker at RHIC (STAR) Collaboration [16] at the Relativistic Heavy Ion Collider (RHIC) [17] reports the first observation of the antimatter hypernucleus ${}^{4}_{\bar{\Lambda}}\overline{\mathrm{H}}$, composed of an $\bar{\Lambda}$, an antiproton and two antineutrons. We also report the measurements of ${}^{3}_{\Lambda}\mathrm{H}$, ${}^{4}_{\Lambda}\mathrm{H}$, ${}^{3}_{\bar{\Lambda}}\overline{\mathrm{H}}$ and ${}^{4}_{\bar{\Lambda}}\overline{\mathrm{H}}$ decay lifetimes, and test matter-antimatter symmetry by hypernucleus-antihypernucleus lifetime comparisons. Various production yield ratios among (anti)hypernuclei and (anti)nuclei are measured and compared with theoretical model predictions, shedding light on the production mechanism of (anti)hypernuclei in relativistic heavy-ion collisions.

(Anti)hypernucleus reconstruction

A total of about 6.4 billion U+U, Au+Au, Ru+Ru, and Zr+Zr collision events with center-of-mass energy per colliding nucleon-nucleon pair $\sqrt{s_{NN}}$=193 GeV (U+U) or 200 GeV (other systems) are used in this analysis. (Anti)hypernuclei ${}^{3}_{\Lambda}\mathrm{H}$, ${}^{3}_{\bar{\Lambda}}\overline{\mathrm{H}}$, ${}^{4}_{\Lambda}\mathrm{H}$ and ${}^{4}_{\bar{\Lambda}}\overline{\mathrm{H}}$ are reconstructed through their two-body decay channels: ${}^{3}_{\Lambda}\mathrm{H}\rightarrow{}^{3}\mathrm{He}+\pi^{-}$, ${}^{3}_{\bar{\Lambda}}\overline{\mathrm{H}}\rightarrow\overline{{}^{3}\mathrm{He}}+\pi^{+}$, ${}^{4}_{\Lambda}\mathrm{H}\rightarrow{}^{4}\mathrm{He}+\pi^{-}$, and ${}^{4}_{\bar{\Lambda}}\overline{\mathrm{H}}\rightarrow\overline{{}^{4}\mathrm{He}}+\pi^{+}$. The charged daughter particles are detected and identified by the cylindrical Time Projection Chamber (TPC) [28] and Time-of-Flight detector (TOF) [29] placed inside the solenoidal magnetic

field of 0.5 Tesla. The TPC reconstructs the three-dimensional tracks and measures their rigidity (momentum over charge) and average ionization energy loss $\langle dE/dx \rangle$ in the gas. Figure 2(A) shows the measured $\langle dE/dx \rangle$ versus the rigidity of charged particles. Bands for different particle species can be seen in the figure. The curves show the expected trends for particles used in this analysis calculated with a Bichsel function [30]. The deviation of the measured $\langle dE/dx \rangle$ from the expected value for a certain particle species normalized by the resolution $\sigma_{dE/dx}$,

$$n_\sigma = \ln\left(\frac{\langle dE/dx \rangle}{\langle dE/dx \rangle_{\text{Bichsel}}}\right)/\sigma_{dE/dx}, \tag{1}$$

is defined and used for particle identification. The squared mass over charge (m^2/Z^2) of a particle is calculated from the rigidity, track length and time of flight measured by the TPC and TOF detectors. n_σ and m^2/Z^2 are used together for the selection of π^+, ^{3}He, ^{4}He and their corresponding antiparticles. Figures 2 (B) and (C) show $n_\sigma(^4\text{He})$ and $n_\sigma(^4\overline{\text{He}})$ versus m^2/Z^2, for the selection of ^{4}He and $^4\overline{\text{He}}$ candidates.

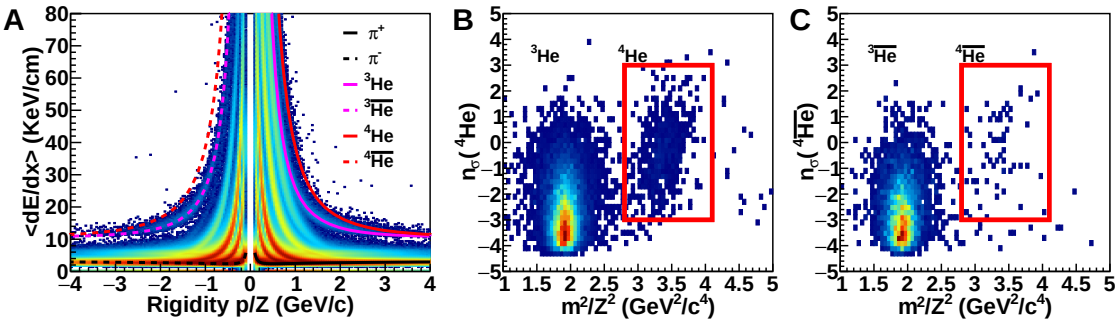

Figure 2: (A) Average energy loss $\langle dE/dx \rangle$ versus rigidity of charged particles measured by the TPC. The lines represent the Bichsel-function calculations for π^+, ^{3}He and ^{4}He and their corresponding antiparticles. (B) and (C) show $n_\sigma(^4\text{He})$ and $n_\sigma(^4\overline{\text{He}})$ versus m^2/Z^2. The red boxes indicate the region for ^{4}He and $^4\overline{\text{He}}$ candidates.

(Anti)hypernucleus candidates are reconstructed from pairs of selected (anti)helium and $\pi^{\pm}$ tracks. In order to suppress background from random combinations of particles emitted from the collision point, selections have been applied such that the tracks of the two daughter particles are likely to come from a common decay vertex with significant displacement from the collision point. The selection cuts on the topological variables are optimized for the best ${}^{3}_{\Lambda}\overline{\mathrm{H}}$ signal.

Signals

To observe the (anti)hypernucleus signals, the invariant mass of their daughter-pair candidates is calculated. The invariant mass is the total energy of the daughter particles in their center-of-mass frame, calculated from their 3-dimensional momenta and masses. According to energy-momentum conservation and Einstein's mass–energy equivalence, the invariant mass of the decay daughters should be equal to the parent-particle mass. The invariant-mass spectra of reconstructed ${}^{3}_{\Lambda}\mathrm{H}$, ${}^{3}_{\Lambda}\overline{\mathrm{H}}$, ${}^{4}_{\Lambda}\mathrm{H}$, and ${}^{4}_{\Lambda}\overline{\mathrm{H}}$ candidates are shown in Fig. 3. The invariant-mass distributions of combinatorial backgrounds are reproduced with a rotation method, in which the (anti)helium nucleus track is randomly rotated around the beam line, so that the decay kinematics of the real signal candidate are destroyed and randomized as the combinatorial background. The final signal count is extracted by subtracting the combinatorial background from the signal distribution within the shaded invariant-mass region in Fig. 3.

In total, 941 ± 59 ${}^{3}_{\Lambda}\mathrm{H}$, 637 ± 49 ${}^{3}_{\Lambda}\overline{\mathrm{H}}$, 24.4 ± 6.1 ${}^{4}_{\Lambda}\mathrm{H}$ and 15.6 ± 4.7 ${}^{4}_{\Lambda}\overline{\mathrm{H}}$ signal candidates are observed. With the signal counts N_{Sig} and background counts N_{Bg} obtained, the significances are

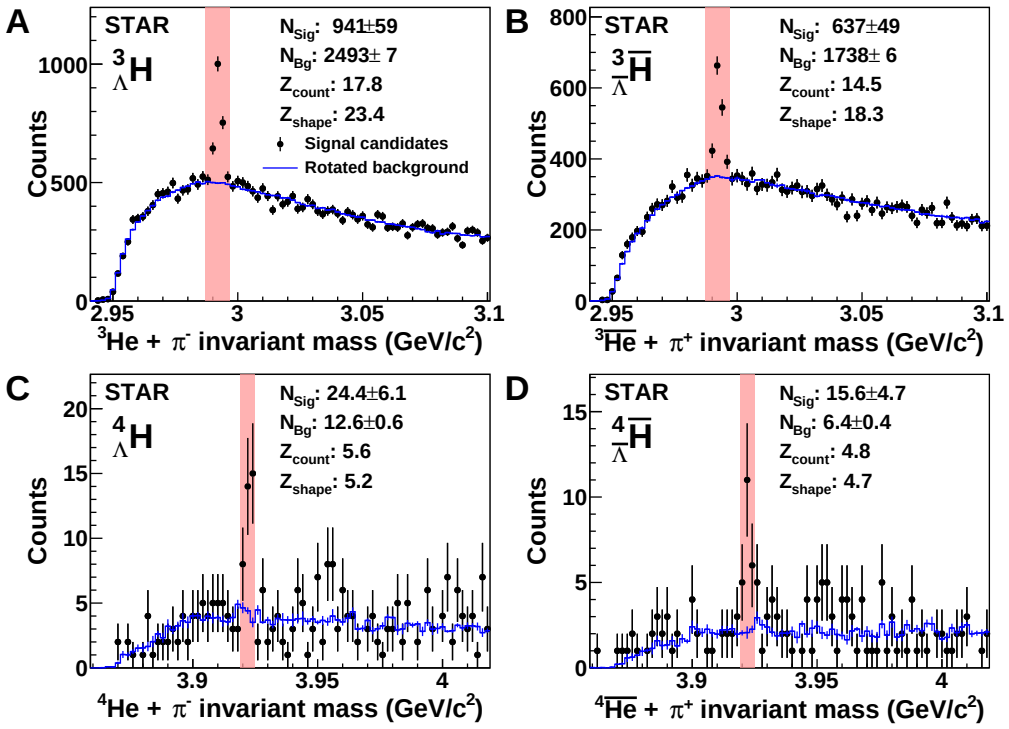

Figure 3: Invariant-mass distributions of $^3\text{He} + \pi^-$ (A), $^3\overline{\text{He}} + \pi^+$ (B), $^4\text{He} + \pi^-$ (C) and $^4\overline{\text{He}} + \pi^+$ (D). The solid bands mark the signal invariant-mass regions. The obtained signal count (N_{Sig}), background count (N_{Bg}), and signal significances (Z_{count} and Z_{shape}) are listed in each panel.

calculated as [31]

$$Z_{\text{count}} = \sqrt{2\left[(N_{\text{Sig}} + N_{\text{Bg}})\ln\left(1 + \frac{N_{\text{Sig}}}{N_{\text{Bg}}}\right) - N_{\text{Sig}}\right]}. \quad (2)$$

The significances Z_{count} of ${}^3_\Lambda\text{H}$, ${}^3_{\overline{\Lambda}}\overline{\text{H}}$, ${}^4_\Lambda\text{H}$, and ${}^4_{\overline{\Lambda}}\overline{\text{H}}$ signals are 17.8, 14.5, 5.6, and 4.8 standard deviations (σ), respectively. The significances are also calculated without setting certain signal invariant-mass regions. Instead, by comparing the likelihoods of fitting the candidate invariant-mass distributions with a Gaussian-shaped signal plus background with the likelihoods with the hypothesis of pure background, the significances Z_{shape} are obtained as 23.4, 18.3, 5.2, and 4.7 σ for ${}^3_\Lambda\text{H}$, ${}^3_{\overline{\Lambda}}\overline{\text{H}}$, ${}^4_\Lambda\text{H}$, and ${}^4_{\overline{\Lambda}}\overline{\text{H}}$, respectively [31].

Lifetimes and matter-antimatter symmetry test

Our current knowledge of physics principles suggests that the initial Universe should have contained equal amounts of matter and antimatter. However, the antiproton flux in cosmic rays and other measurements [32] indicate that no large-scale antimatter exists in the vicinity of our galaxy, and the visible universe is almost entirely matter. Naturally, one may ask where the antimatter is, and what causes this matter-antimatter asymmetry in the Universe? Quantum physics expects a matter particle and its corresponding antimatter particle to have the same properties according to the CPT theorem, which states that physical laws should remain unchanged under the combined operation of charge conjugation C, parity transformation P and time reversal T [33]. Comparing the properties like mass and lifetime of a particle and its corresponding antiparticle is an important experimental way to test the CPT symmetry [34] and to search for new mechanisms that cause matter and antimatter asymmetry in the Universe. Recently, the ALICE and STAR experiments reported that there is no significant mass (binding energy) difference between deuteron and antideuteron [13], between ^{3}He and $^3\overline{\mathrm{He}}$ [13] and between ${}^3_\Lambda\mathrm{H}$ and ${}^3_{\bar{\Lambda}}\overline{\mathrm{H}}$ [10]. ALICE has also measured the relative difference between ${}^3_\Lambda\mathrm{H}$ and ${}^3_{\bar{\Lambda}}\overline{\mathrm{H}}$ lifetimes, which is consistent with zero [35].

Hypernucleus lifetimes are also a good probe to study the interactions between the hyperons and nucleons within them [36], which is an important nuclear physics input for understanding the inner structure of compact stellar objects like neutron stars [37]. Numerous measurements of the lifetimes of hypernuclei [11,38–47] show slightly shorter average lifetimes of ${}^3_\Lambda\mathrm{H}$ and ${}^4_\Lambda\mathrm{H}$ than that of the Λ hyperon. The combined lifetime of ${}^3_\Lambda\mathrm{H}$ and ${}^3_{\bar{\Lambda}}\overline{\mathrm{H}}$ has also been measured [7,35,45,48].

In this study, lifetimes of the (anti)hypernuclei ${}^{3}_{\Lambda}\mathrm{H}$, ${}^{4}_{\Lambda}\mathrm{H}$, ${}^{3}_{\bar{\Lambda}}\overline{\mathrm{H}}$ and ${}^{4}_{\bar{\Lambda}}\overline{\mathrm{H}}$ are measured. In order to avoid the low transverse momentum (p_T) region, where the reconstruction efficiency approaches zero and may have relatively large systematic uncertainties, the measurement is performed only for (anti)hypernuclei with $p_T > 2.1$ GeV/c. (Anti)hypernucleus signal yields in $ct = L/\beta\gamma = L/(p/m)$ intervals are obtained as described in the section above, where c, t, L, β, γ, p and m represent the speed of light, the decay time in the (anti)hypernucleus rest frame, the measured decay length, the ratio of velocity to c, the Lorentz factor of relativistic time dilation, the measured momentum and the (anti)hypernucleus nominal mass [49], respectively. The reconstruction efficiencies of ${}^{3}_{\Lambda}\mathrm{H}$, ${}^{3}_{\bar{\Lambda}}\overline{\mathrm{H}}$, ${}^{4}_{\Lambda}\mathrm{H}$ and ${}^{4}_{\bar{\Lambda}}\overline{\mathrm{H}}$ in each $L/\beta\gamma$ bin are evaluated by a Monte Carlo method in which (anti)hypernuclei are simulated using the GEANT3 [50] software package and embedded in real collision events. In this way, the simulated (anti)hypernuclei are reconstructed in a realistic environment. Efficiency-corrected yields of ${}^{3}_{\Lambda}\mathrm{H}$, ${}^{3}_{\bar{\Lambda}}\overline{\mathrm{H}}$, ${}^{4}_{\Lambda}\mathrm{H}$ and ${}^{4}_{\bar{\Lambda}}\overline{\mathrm{H}}$ as a function of $L/\beta\gamma$ are shown in Fig.4(A). The lifetimes τ are extracted by fitting the data with the expression $N(t) = N_0 \exp(-t/\tau) = N_0 \exp(-(L/\beta\gamma)/c\tau)$.

The extracted ${}^{3}_{\Lambda}\mathrm{H}$, ${}^{3}_{\bar{\Lambda}}\overline{\mathrm{H}}$, ${}^{4}_{\Lambda}\mathrm{H}$ and ${}^{4}_{\bar{\Lambda}}\overline{\mathrm{H}}$ lifetimes are shown in Fig. 4(B). Within uncertainties, our results are consistent with most existing measurements[7,11,35,38–48] and theory predictions [52–57]. The lifetime differences between hypernuclei and their corresponding antihypernuclei are $\tau\left({}^{3}_{\Lambda}\mathrm{H}\right) - \tau\left({}^{3}_{\bar{\Lambda}}\overline{\mathrm{H}}\right) = [16 \pm 43(\mathrm{stat.}) \pm 20(\mathrm{sys.})]$ ps and $\tau\left({}^{4}_{\Lambda}\mathrm{H}\right) - \tau\left({}^{4}_{\bar{\Lambda}}\overline{\mathrm{H}}\right) = [18 \pm 115(\mathrm{stat.}) \pm 46(\mathrm{sys.})]$ ps. Both are consistent with zero within uncertainties. This is a new test of the matter-antimatter and CPT symmetry.

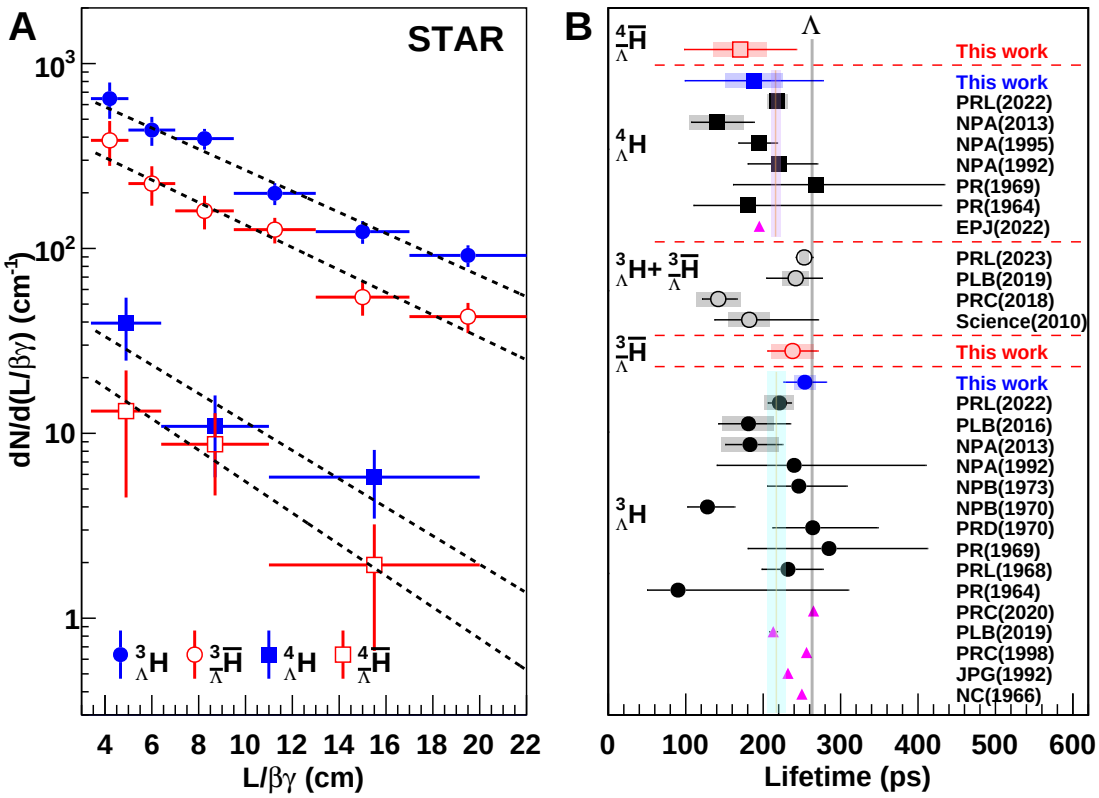

Figure 4: (A) ${}^{3}_{\Lambda}\mathrm{H}$, ${}^{3}_{\Lambda}\overline{\mathrm{H}}$, ${}^{4}_{\Lambda}\mathrm{H}$ and ${}^{4}_{\Lambda}\overline{\mathrm{H}}$ yields versus $L/\beta\gamma$. The vertical error bars represent the statistical uncertainties only. (B) Our measured ${}^{3}_{\Lambda}\mathrm{H}$, ${}^{3}_{\Lambda}\overline{\mathrm{H}}$, ${}^{4}_{\Lambda}\mathrm{H}$ and ${}^{4}_{\Lambda}\overline{\mathrm{H}}$ lifetimes compared with world data [7,11,35,38–48,51] and theoretical predictions [52–57] (solid triangles). Error bars and boxes represent statistical and systematic uncertainties, respectively. Solid vertical lines with shaded regions show the average lifetimes of ${}^{3}_{\Lambda}\mathrm{H}$ and ${}^{4}_{\Lambda}\mathrm{H}$ and their corresponding uncertainties calculated from previous results. The vertical gray line shows the lifetime of the free Λ[34].

Yield ratios

The (anti)nucleus and (anti)hypernucleus production yields are sensitive to their production mechanism in relativistic heavy-ion collisions. Collisions at RHIC energies create fireballs with a temperature of several hundred MeV [58], or on the order of 10^{12} K, while the (anti)nuclei and (anti)hypernuclei have typical binding energies of merely several MeV per (anti)baryon. Thus, it is commonly believed that these fragile objects are produced at the last stage of the collision-system evolution, via coalescence of (anti)hyperons and (anti)nucleons that are by chance close in both coordinate and momentum space [59–61]. As observed in earlier measurements [8,12], the probability to coalesce decreases by 2-3 orders of magnitude with each additional (anti)baryon. Since the strange quarks are heavier than up and down quarks, they take more energy to be created. There are fewer strange quarks than up and down quarks in the fireballs, thus (anti)hypernucleus production yields are usually lower than those of (anti)nuclei with the same baryon numbers [7,11]. These baryon number and strangeness dependencies of particle production yields can also be well described by the statistical thermal model [58], which assumes all particles to be in a thermal and chemical equilibrium. The chemical freeze-out temperature T and baryon chemical potential μ_B parameters in the statistical thermal model can be obtained by a simultaneous fit to all existing measured particle yields.

This analysis uses a combination of data from different collision systems, with different particle production yields. Thus the absolute (anti)hypernuclear production yields in this mixture of collisions are not well-defined physics quantities to measure. Instead, we measure various yield

ratios between particles with the same baryon number. In this way, the yield differences due to different collision-system sizes will largely cancel out. The measurement is done with particles in a phase-space region of rapidity $|y| < 0.7$ and $0.7 < p_T/m < 1.5$. Detector acceptance, efficiency and decay branching fractions are corrected for. Following the conventions in previous analyses [7,11,46,62], we use 0.25 as the decay branching fraction of ${}^{3}_{\Lambda}\mathrm{H}\rightarrow{}^{3}\mathrm{He}+\pi^{-}$and ${}^{3}_{\bar{\Lambda}}\overline{\mathrm{H}}\rightarrow{}^{3}\overline{\mathrm{He}}+\pi^{+}$ [54,63], and 0.5 for ${}^{4}_{\Lambda}\mathrm{H}\rightarrow{}^{4}\mathrm{He}+\pi^{-}$and ${}^{4}_{\bar{\Lambda}}\overline{\mathrm{H}}\rightarrow{}^{4}\overline{\mathrm{He}}+\pi^{+}$ [64,65]. ${}^{3}\mathrm{He}$, ${}^{3}\overline{\mathrm{He}}$, ${}^{4}\mathrm{He}$, and ${}^{4}\overline{\mathrm{He}}$ yields are corrected for contributions from ${}^{3}_{\Lambda}\mathrm{H}$, ${}^{3}_{\bar{\Lambda}}\overline{\mathrm{H}}$, ${}^{4}_{\Lambda}\mathrm{H}$, and ${}^{4}_{\bar{\Lambda}}\overline{\mathrm{H}}$ decays when calculating the ratios.

Figure 5 shows the measured particle production yield ratios and a comparison to previous experimental results[7,8,11,66], as well as the statistical thermal model predictions[58]. Since the ${}^{3}_{\Lambda}\mathrm{H}/{}^{3}\mathrm{He}$ and ${}^{3}_{\bar{\Lambda}}\overline{\mathrm{H}}/{}^{3}\overline{\mathrm{He}}$ ratios are expected to increase with the collision-system size[67,68], we have also conducted the measurement of them in large (U+U, Au+Au) and small (Zr+Zr, Ru+Ru) systems separately, in order to compare with existing measurements. The measured particle ratios are consistent with previous measurements, while we note that the ${}^{3}_{\Lambda}\mathrm{H}/{}^{3}\mathrm{He}$ and ${}^{3}_{\bar{\Lambda}}\overline{\mathrm{H}}/{}^{3}\overline{\mathrm{He}}$ ratios in U+U and Au+Au collisions are lower than previous STAR results [7] by 2.8 and 1.9 σ, respectively.

Various antimatter-over-matter particle-yield ratios are measured to be below unity because the colliding heavy-ions carry positive baryon numbers, and consequently the collision system has positive baryon chemical potential. We also observe that ${}^{4}\overline{\mathrm{He}}/{}^{4}\mathrm{He} \sim {}^{3}\overline{\mathrm{He}}/{}^{3}\mathrm{He} \times \overline{\mathrm{p}}/\mathrm{p}$, ${}^{4}_{\bar{\Lambda}}\overline{\mathrm{H}}/{}^{4}_{\Lambda}\mathrm{H} \sim {}^{3}_{\bar{\Lambda}}\overline{\mathrm{H}}/{}^{3}_{\Lambda}\mathrm{H} \times \overline{\mathrm{p}}/\mathrm{p}$, ${}^{4}_{\Lambda}\mathrm{H}/{}^{4}\mathrm{He} \sim 4 \times {}^{3}_{\Lambda}\mathrm{H}/{}^{3}\mathrm{He}$, and ${}^{4}_{\bar{\Lambda}}\overline{\mathrm{H}}/{}^{4}\overline{\mathrm{He}} \sim 4 \times {}^{3}_{\bar{\Lambda}}\overline{\mathrm{H}}/{}^{3}\overline{\mathrm{He}}$, as expected in the coalescence [59,60] picture of (anti)nucleus and (anti)hypernucleus production. Here the factors 4 are introduced because both spin-0 and spin-1 states of ${}^{4}_{\Lambda}\mathrm{H}$ have enough binding energy so that no

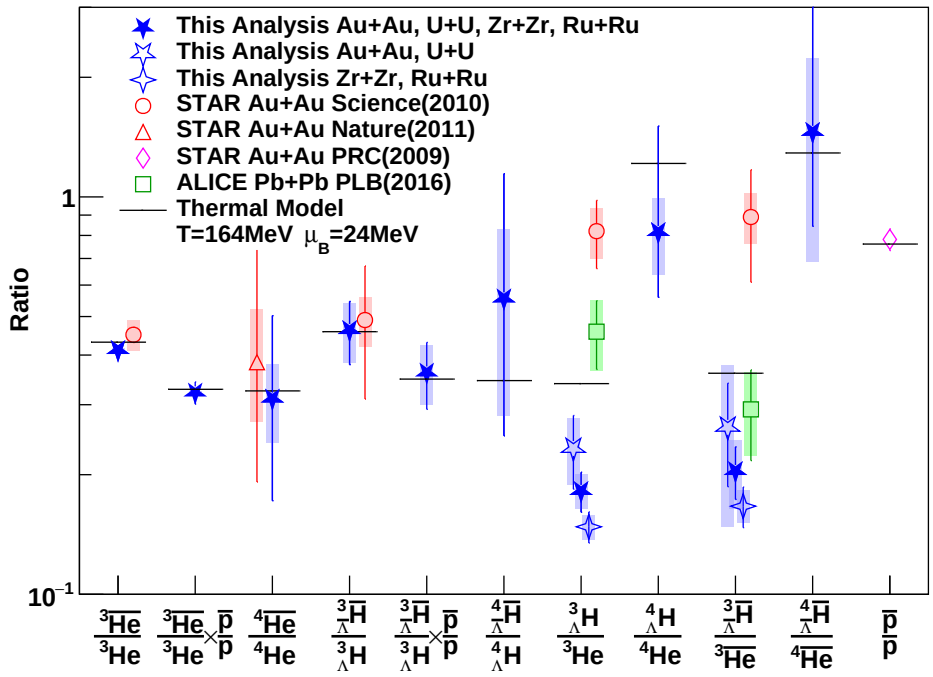

Figure 5: Production-yield ratios of various particles with the same baryon number. Results combining all collision systems in this work are shown by filled stars. Open stars show results with only U+U and Au+Au collisions, while quadrangular stars show results with only Zr+Zr and Ru+Ru collisions. Statistical uncertainties and systematic uncertainties are shown by vertical bars and shaded boxes, respectively. The decay branching fraction of ${}^{3}_{\Lambda}\mathrm{H}\rightarrow{}^{3}\mathrm{He}+\pi^{-}$ and ${}^{3}_{\Lambda}\overline{\mathrm{H}}\rightarrow{}^{3}\overline{\mathrm{He}}+\pi^{+}$ is assumed to be 0.25 [54,63], and the branching fraction of ${}^{4}_{\Lambda}\mathrm{H}\rightarrow{}^{4}\mathrm{He}+\pi^{-}$ and ${}^{4}_{\Lambda}\overline{\mathrm{H}}\rightarrow{}^{4}\overline{\mathrm{He}}+\pi^{+}$ is assumed to be 0.5 [64,65]. Previous measurement results [7,8,11,66] and statistical-thermal-model predictions [58] are also shown for comparison.

energetically allowed strong decay channels exist for them. So the spin-1 state, with a spin degeneracy of 3, will decay electromagnetically to the spin-0 ground state. This enhances the total measured ${}^{4}_{\Lambda}\mathrm{H}$ and ${}^{4}_{\bar{\Lambda}}\overline{\mathrm{H}}$ production yield by a factor of 4, compared to ${}^{4}\mathrm{He}$ and ${}^{4}\overline{\mathrm{He}}$ which have only a spin-0 state [46,49,69,70]. Considering this spin-degeneracy effect, the statistical-thermal-model [58] predictions also match our measurements, except that the measured ${}^{3}_{\Lambda}\mathrm{H}/{}^{3}\mathrm{He}$ ratio is slightly lower than the statistical-thermal-model prediction. This difference, if really exists, may be explained by the very small binding energy of ${}^{3}_{\Lambda}\mathrm{H}$, which implies the wave-function size of ${}^{3}_{\Lambda}\mathrm{H}$ is comparable to the whole collision system [67,68,71].

In general, our measured particle yield ratios are consistent with the expectation of the coalescence picture of (anti)nucleus and (anti)hypernucleus production and the statistical thermal model. Despite an enhancement factor of 4 due to the spin-degeneracy effect, the ${}^{4}_{\bar{\Lambda}}\overline{\mathrm{H}}$ production yield is still about 2 orders of magnitude lower than that of ${}^{3}_{\bar{\Lambda}}\overline{\mathrm{H}}$ [61]. Fourteen years after the discovery of the first antihypernucleus ${}^{3}_{\bar{\Lambda}}\overline{\mathrm{H}}$, 15.6 ${}^{4}_{\bar{\Lambda}}\overline{\mathrm{H}}$ signal candidates are reconstructed and identified out of 6.4 billion collision events in this study, which is a great step forward in the experimental research of antimatter.

Acknowledgement

We thank the RHIC Operations Group and RCF at BNL, the NERSC Center at LBNL, and the Open Science Grid consortium for providing resources and support. This work was supported in part by the Office of Nuclear Physics within the U.S. DOE Office of Science, the U.S. National

Science Foundation, National Natural Science Foundation of China, Chinese Academy of Science, the Ministry of Science and Technology of China and the Chinese Ministry of Education, the Higher Education Sprout Project by Ministry of Education at NCKU, the National Research Foundation of Korea, Czech Science Foundation and Ministry of Education, Youth and Sports of the Czech Republic, Hungarian National Research, Development and Innovation Office, New National Excellency Programme of the Hungarian Ministry of Human Capacities, Department of Atomic Energy and Department of Science and Technology of the Government of India, the National Science Centre and WUT ID-UB of Poland, the Ministry of Science, Education and Sports of the Republic of Croatia, German Bundesministerium für Bildung, Wissenschaft, Forschung and Technologie (BMBF), Helmholtz Association, Ministry of Education, Culture, Sports, Science, and Technology (MEXT) and Japan Society for the Promotion of Science (JSPS).

Data availability

All raw data for this study were collected using the STAR detector at Brookhaven National Laboratory and are not available to the public. Derived data supporting the findings of this study are publicly available in the HEPData repository (The webpage link will be provided before the final publication of the paper.) or from the corresponding author on request.

Code availability

The codes to process raw data collected by the STAR detector are publicly available at https://github.com/star-bnl. The codes to analyse the produced data are not publicly available.

Reference

1. Adams, J. *et al.* Experimental and Theoretical Challenges in the Search for the Quark Gluon Plasma: The STAR Collaboration's Critical Assessment of the Evidence from RHIC Collisions. *Nucl. Phys. A* **757**, 102–183 (2005). nucl-ex/0501009.

2. Adcox, K. *et al.* Formation of Dense Partonic Matter in Relativistic Nucleus-Nucleus Collisions at RHIC: Experimental Evaluation by the PHENIX Collaboration. *Nucl. Phys. A* **757**, 184–283 (2005). nucl-ex/0410003.

3. Back, B. B. *et al.* The PHOBOS Perspective on Discoveries at RHIC. *Nucl. Phys. A* **757**, 28–101 (2005). nucl-ex/0410022.

4. Arsene, I. *et al.* Quark Gluon Plasma and Color Glass Condensate at RHIC: The Perspective from the BRAHMS Experiment. *Nucl. Phys. A* **757**, 1–27 (2005). nucl-ex/0410020.

5. Muller, B., Schukraft, J. & Wyslouch, B. First Results from Pb+Pb Collisions at the LHC. *Ann. Rev. Nucl. Part. Sci.* **62**, 361–386 (2012). 1202.3233.

6. Adam, J. *et al.* Beam energy dependence of (anti-)deuteron production in Au + Au collisions at the BNL Relativistic Heavy Ion Collider. *Phys. Rev. C* **99**, 064905 (2019). 1903.11778.

7. Abelev, B. I. *et al.* Observation of an Antimatter Hypernucleus. *Science* **328**, 58–62 (2010). 1003.2030.

8. Agakishiev, H. *et al.* Observation of the Antimatter Helium-4 Nucleus. *Nature* **473**, 353 (2011). [Erratum: Nature 475, 412 (2011)], 1103.3312.

9. Chen, J., Keane, D., Ma, Y.-G., Tang, A. & Xu, Z. Antinuclei in Heavy-Ion Collisions. *Phys. Rept.* **760**, 1–39 (2018). 1808.09619.

10. Adam, J. *et al.* Measurement of the Mass Difference and the Binding Energy of the Hypertriton and Antihypertriton. *Nature Phys.* **16**, 409–412 (2020). 1904.10520.

11. Adam, J. *et al.* ${}^{3}_{\Lambda}\mathrm{H}$ and ${}^{3}_{\Lambda}\overline{\mathrm{H}}$ Production in Pb-Pb Collisions at $\sqrt{s_{\mathrm{NN}}} = 2.76$ TeV. *Phys. Lett. B* **754**, 360–372 (2016). 1506.08453.

12. Acharya, S. *et al.* Production of ${}^{4}\mathrm{He}$ and ${}^{4}\overline{\mathrm{He}}$ in Pb-Pb Collisions at $\sqrt{s_{\mathrm{NN}}}$ = 2.76 TeV at the LHC. *Nucl. Phys. A* **971**, 1–20 (2018). 1710.07531.

13. Adam, J. *et al.* Precision Measurement of the Mass Difference between Light Nuclei and Anti-nuclei. *Nature Phys.* **11**, 811–814 (2015). 1508.03986.

14. Braun-Munzinger, P. & Dönigus, B. Loosely-bound objects produced in nuclear collisions at the LHC. *Nucl. Phys. A* **987**, 144–201 (2019). 1809.04681.

15. Dönigus, B. Selected highlights of the production of light (anti-)(hyper-)nuclei in ultra-relativistic heavy-ion collisions. *Eur. Phys. J. A* **56**, 280 (2020).

16. Ackermann, K. *et al.* STAR Detector Overview. *Nuclear Instruments and Methods A* **499**, 624–632 (2003).

17. Harrison, M., Ludlam, T. & Ozaki, S. RHIC project overview. *Nucl. Instrum. Meth. A* **499**, 235–244 (2003).

18. Dirac, P. A. The Quantum Theory of the Electron. *Proc. Roy. Soc. Lond. A* **117**, 610–624 (1928).

19. Dirac, P. A. Quantised Singularities in the Electromagnetic Field. *Proc. Roy. Soc. Lond. A* **133**, 60–72 (1931).

20. Anderson, C. The Positive Electron. *Phys. Rev.* **43**, 491–494 (1933).

21. Chamberlain, O., Segre, E., Wiegand, C. & Ypsilantis, T. Observation of Anti-Protons. *Phys. Rev.* **100**, 947–950 (1955).

22. Cork, B., Lambertson, G. R., Piccioni, O. & Wenzel, W. A. Anti-neutrons Produced from Anti-protons in Charge Exchange Collisions. *Phys. Rev.* **104**, 1193–1197 (1957).

23. Prowse, D. J. & Baldo-Ceolin, M. Anti-lambda hyperon. *Phys. Rev. Lett.* **1**, 179–180 (1958).

24. Massam, T., Muller, T., Righini, B., Schneegans, M. & Zichichi, A. Experimental Observation of Antideuteron Production. *Nuovo Cim.* **39**, 10–14 (1965).

25. Dorfan, D. E., Eades, J., Lederman, L. M., Lee, W. & Ting, C. C. Observation of Antideuterons. *Phys. Rev. Lett.* **14**, 1003–1006 (1965).

26. Antipov, Y. M. *et al.* Observation of Anti-he-3. *Yad. Fiz.* **12**, 311–322 (1970).

27. Vishnevsky, N. K. *et al.* Observation of Anti-Tritium. *Yad. Fiz.* **20**, 694–708 (1974).

28. Anderson, M. *et al.* The STAR Time Projection Chamber: a Unique Tool for Studying High Multiplicity Events at RHIC. *Nuclear Instruments and Methods A* **499**, 659–678 (2003).

29. Llope, W. J. and STAR collaboration et al. Multigap RPCs in the STAR Experiment at RHIC. *Nuclear Instruments and Methods A* **661**, S110–S113 (2012).

30. Bichsel, H. A Method to Improve Tracking and Particle Identification in TPCs and Silicon Detectors. *Nuclear Instruments and Methods A* **562**, 154–197 (2006).

31. Cowan, G., Cranmer, K., Gross, E. & Vitells, O. Asymptotic formulae for likelihood-based tests of new physics. *Eur. Phys. J. C* **71**, 1554 (2011). [Erratum: Eur.Phys.J.C 73, 2501 (2013)], 1007.1727.

32. Aguilar, M. *et al.* Antiproton Flux, Antiproton-to-Proton Flux Ratio, and Properties of Elementary Particle Fluxes in Primary Cosmic Rays Measured with the Alpha Magnetic Spectrometer on the International Space Station. *Phys. Rev. Lett.* **117**, 091103 (2016).

33. Luders, G. On the Equivalence of Invariance under Time Reversal and under Particle-Antiparticle Conjugation for Relativistic Field Theories. *Kong. Dan. Vid. Sel. Mat. Fys. Med.* **28N5**, 1–17 (1954).

34. Group, P. D. *et al.* Review of Particle Physics. *Progress of Theoretical and Experimental Physics* **2022**, 083C01 (2022).

35. Acharya, S. *et al.* Measurement of the Lifetime and Λ Separation Energy of ${}^{3}_{\Lambda}\mathrm{H}$. *Phys. Rev. Lett.* **131**, 102302 (2023). 2209.07360.

36. Pérez-Obiol, A., Gazda, D., Friedman, E. & Gal, A. Revisiting the hypertriton lifetime puzzle. *Physics Letters B* **811**, 135916 (2020).

37. Gal, A., Hungerford, E. V. & Millener, D. J. Strangeness in Nuclear Physics. *Rev. Mod. Phys.* **88**, 035004 (2016).

38. Prem, R. J. *et al.* Lifetimes of Hypernuclei, ${}^{3}_{\Lambda}\mathrm{H}$, ${}^{4}_{\Lambda}\mathrm{H}$, ${}^{5}_{\Lambda}\mathrm{H}$. *Phys. Rev.* **136**, B1803 (1964).

39. Keyes, G. *et al.* New Measurement of the ${}^{3}_{\Lambda}\mathrm{H}$. *Phys. Rev. Lett.* **20**, 819–821 (1968).

40. Phillips, R. E. *et al.* Lifetimes of Light Hyperfragments. II. *Phys. Rev.* **180**, 1307 (1964).

41. Keys, G. *et al.* Properties of ${}^{3}_{\Lambda}\mathrm{H}$. *Phys. Rev. D* **1**, 66–77 (1970).

42. Keys, G. *et al.* A Measurement of the Lifetime of the ${}^{3}_{\Lambda}\mathrm{H}$ Hypernucleus. *Nucl. Phys. B* **67**, 269–283 (1973).

43. Avramenko, S. *et al.* A Study of the Production and Lifetime of the Lightest Relativistic Hypernuclei. *Nucl. Phys. A* **547**, 95c (1992).

44. Rappold, C. *et al.* Hypernuclear Spectroscopy of Products from ^{6}Li Projectiles on a Carbon Target at 2 A GeV. *Nucl. Phys. A* **913**, 170–184 (2013).

45. Adamczyk, L. *et al.* Measurement of the ${}^{3}_{\Lambda}\mathrm{H}$ lifetime in Au+Au collisions at the BNL Relativistic Heavy Ion Collider. *Phys. Rev. C* **97**, 054909 (2018). 1710.00436.

46. Abdallah, M. *et al.* Measurements of ${}^{3}_{\Lambda}\mathrm{H}$ and ${}^{4}_{\Lambda}\mathrm{H}$ Lifetimes and Yields in Au+Au Collisions in the High Baryon Density Region. *Phys. Rev. Lett.* **128**, 202301 (2022). 2110.09513.

47. Outa, H. *et al.* Mesonic Weak Decay of ${}^{4}_{\Lambda}\mathrm{H}$ and ${}^{4}_{\Lambda}\mathrm{He}$. *Nucl. Phys. A* **585**, 109c (1995).

48. Acharya, S. *et al.* ${}^{3}_{\Lambda}\mathrm{H}$ and ${}^{3}_{\Lambda}\overline{\mathrm{H}}$ lifetime measurement in Pb-Pb collisions at $\sqrt{s_{\mathrm{NN}}} = 5.02$ TeV via two-body decay. *Phys. Lett. B* **797**, 134905 (2019). 1907.06906.

49. Eckert, P., Achenbach, P. *et al.* Chart of hypernuclides — hypernuclear structure and decay data (2021). Https://hypernuclei.kph.uni-mainz.de.

50. Brun, R., Bruyant, F., Maire, M., McPherson, A. C. & Zanarini, P. GEANT3 (1987).

51. Bohm, G. *et al.* On the lifetime of the ${}^{3}_{\Lambda}\mathrm{H}$ hypernucleus. *Nucl. Phys. B* **16**, 46–52 (1970). [Erratum: Nucl.Phys.B 16, 523–523 (1970)].

52. Rayet, M. & Dalitz, R. H. The Lifetime of ${}^{3}_{\Lambda}\mathrm{H}$. *Nuovo Cimento* **XLVI**, 8302–8310 (1966).

53. Congleton, J. G. A Simple Model of the Hypertriton. *J. Phys. G: Nucl. Part. Phys.* **18**, 339–357 (1992).

54. Kamada, H. *et al.* π-mesonic Decay of the Hypertriton. *Phys. Rev. C* **57**, 1595–1603 (1998).

55. Gal, A. *et al.* Towards Resolving the ${}^{3}_{\Lambda}\mathrm{H}$ Lifetime Puzzle. *Phys. Lett. B* **791**, 48–53 (2019).

56. Hildenbrand, F. & Hammer, H.-W. Lifetime of the Hypertriton. *Phys. Rev. C* **102**, 064002 (2020).

57. Gal, A. Recent Progress on few-body Hypernuclei. *EPJ Web Conf.* **259**, 08002 (2022).

58. Andronic, A., Braun-Munzinger, P., Stachel, J. & Stöcker, H. Production of Light Nuclei, Hypernuclei and Their Antiparticles in Relativistic Nuclear Collisions. *Phys. Lett. B* **697**, 203–207 (2011).

59. Sato, H. & Yazaki, K. On the Coalescence Model for High Energy Nuclear Reactions. *Phys. Lett. B* **98**, 153–157 (1981).

60. Steinheimer, J. *et al.* Hypernuclei, Dibaryon and Antinuclei Production in High Energy Heavy Ion Collisions: Thermal Production vs. Coalescence. *Phys. Lett. B* **714**, 85–91 (2012).

61. Sun, K.-J. & Chen, L.-W. Antimatter ${}^{4}_{\Lambda}\mathrm{H}$ Hypernucleus Production and the ${}^{3}_{\Lambda}\mathrm{H}/{}^{3}\mathrm{He}$ Puzzle in Relativistic Heavy-Ion Collisions. *Phys. Rev. C* **93**, 064909 (2016). 1512.00692.

62. Armstrong, T. A. *et al.* Production of H**3(Lambda) and H**4(Lambda) in central 11.5-GeV/c Au + Pt heavy ion collisions. *Phys. Rev. C* **70**, 024902 (2004). nucl-ex/0211010.

63. Glöckle, W., Miyagawa, K., Kamada, H., Golak, J. & Witala, H. The hypertriton and its decays. *Nucl. Phys. A* **639**, 297c–306c (1998).

64. Kumagai-Fuse, I., Okabe, S. & Akaishi, Y. Pauli effects on pionic decay of light Lambda hypernuclei. *Nucl. Phys. A* **585**, 365c–366c (1995).

65. Outa, H. *et al.* Mesonic and non-mesonic decay widths of (Lambda)H-4 and (Lambda)He-4. *Nucl. Phys. A* **639**, 251c–260c (1998).

66. Abelev, B. I. *et al.* Identified Baryon and Meson Distributions at Large Transverse Momenta from Au+Au Collisions at $\sqrt{s_{NN}} = 200$ GeV. *Phys. Rev. Lett.* **97**, 152301 (2006). nucl-ex/0606003.

67. Sun, K.-J., Ko, C. M. & Dönigus, B. Suppression of light nuclei production in collisions of small systems at the Large Hadron Collider. *Phys. Lett. B* **792**, 132–137 (2019). 1812.05175.

68. Bellini, F. & Kalweit, A. P. Testing production scenarios for (anti-)(hyper-)nuclei and exotica at energies available at the CERN Large Hadron Collider. *Phys. Rev. C* **99**, 054905 (2019). 1807.05894.

69. Vovchenko, V., Dönigus, B., Kardan, B., Lorenz, M. & Stoecker, H. Feeddown contributions from unstable nuclei in relativistic heavy-ion collisions. *Phys. Lett.* **B**, 135746 (2020). 2004.04411.

70. Dönigus, B. Hypernuclei at relativistic energies. *EPJ Web Conf.* **276**, 04002 (2023).

71. Armstrong, T. A. *et al.* Mass Dependence of Light Nucleus Production in Ultrarelativistic Heavy Ion Collisions. *Phys. Rev. Lett.* **83**, 5431–5434 (1999). nucl-ex/9907002.

Methods

Event Sample and Trigger Selection. This analysis used 606 million and 624 million $\sqrt{s_{NN}} = 200$ GeV Au+Au collision events obtained in years 2010 and 2011, 512 million $\sqrt{s_{NN}} = 193$ GeV U+U collision events from year 2012, and 4.7 billion $\sqrt{s_{NN}} = 200$ GeV Ru+Ru and Zr+Zr collision events from year 2018.

The majority of events were collected with minimum-bias (MB) triggers. The MB trigger is designed to accept the events with different impact parameters as equally as possible. The MB triggers required a coincidence between either the vertex-position detectors (VPD) or the zero-degree calorimeters (ZDC). The VPD [1] is a pair of timing detectors mounted directly around the beampipe that cover approximately half of the phase space over the pseudorapidity region $4.2 < |\eta| < 5.2$. The ZDC [2] is a pair of hadronic calorimeters located at $|\eta| > 6.6$ that detect spectator neutrons emerging from the heavy-ion collisions.

Often the MB triggers were highly prescaled to reserve a fraction of the data-acquisition bandwidth for triggers on rare processes. Events that satisfied "central" or "non-photonic electron" triggers were included in the analysis to enhance the overall statistics. The central triggers combined multiplicity information from the time-of-flight system [3] with spectator-neutron multiplicity information from the ZDCs to select collisions with small impact parameters. The non-photonic electron triggers, intended primarily to select events containing electrons from charm- and bottom-quark decays, required a large transverse energy deposition ($E_T > 2.6$, 3.5, or 4.2 GeV) in at least one $\Delta\eta \times \Delta\phi = 0.05 \times 0.05$ tower in the barrel electromagnetic calorimeter [4]. They have a high

probability to trigger on events containing antinuclei, which may annihilate in the electromagnetic calorimeter. Events triggered by the "central" or "non-photonic electron" triggers were not used in the yield ratios analysis to avoid potential biases.

The reconstructed collision point, called the primary vertex, is required to be within 2 cm of the beam line and within 40 cm along the beam line from the detector center.

Daughter-Particle Identification. Information from the TPC and the TOF are combined for particle identification. The cylindrical TPC has full azimuthal coverage in the pseudorapidity range $-1 < \eta < 1$. In order to ensure good track quality, a minimum of 20 measured points in TPC is required for all tracks used in this analysis. A selected ^{3}He or $^3\overline{\text{He}}$ candidate should satisfy $|n_{\sigma^3\text{He}}| < 3$. If the track has matched TOF hit information, it should also satisfy the condition $1.0 < m^2/Z^2 < 3.0$ (GeV/c^2)^2. For ^{4}He and $^4\overline{\text{He}}$ selection, in addition to $|n_{\sigma^4\text{He}}| < 3$, it is also required that $2.8 < m^2/Z^2 < 4.1$ (GeV/c^2)^2 if a matching TOF hit is present or $|n_{\sigma^3\text{He}}| > 3.5$ if there is no TOF match, in order to minimize contamination from ^{3}He and $^3\overline{\text{He}}$, which have much higher production yields. In order to reject background ^{3}He and ^{4}He knocked out from the beam pipe and other materials, the distance-of-closest approach (DCA) between the ^{3}He or ^{4}He trajectory and the primary vertex is required to be within 1 cm. This DCA requirement is not applied to $^3\overline{\text{He}}$ and $^4\overline{\text{He}}$ since there are no knock-out antinuclei. The daughter $\pi^\pm$ from (anti)hypernucleus decay is identified by requiring $|n_{\sigma\pi^\pm}| < 3$. A m^2/Z^2 cut is also applied if the track is associated with a TOF hit.

Topological Reconstruction. (Anti)hypernucleus candidates are reconstructed from the selected $\pi^{\pm}$ and (anti)helium nucleus tracks by the Kalman-Filter (KF) Particle Finder package [5–8], which is based on the Kalman filter method. The decay topology of a hypernucleus, as illustrated in Fig. 1, is characterized by several variables: χ^2_{topo} describing the likelihood that the path of the reconstructed mother particle goes through the primary vertex, χ^2_{NDF} describing the likelihood that the two daughter tracks come from a common decay vertex, $\chi^2_{primary}$ describing the likelihood that the decay-daughter track comes from the primary vertex, the decay length (L), and L over its uncertainty (L/dL). The selection cuts on these topological variables are optimized for the best ${}^{3}_{\Lambda}\overline{\mathrm{H}}$ signal, instead of ${}^{4}_{\Lambda}\overline{\mathrm{H}}$ signal, in order to avoid any bias towards a better signal and a larger yield of ${}^{4}_{\Lambda}\overline{\mathrm{H}}$ due to statistical fluctuations. This bias due to fluctuations is much smaller for ${}^{3}_{\Lambda}\overline{\mathrm{H}}$ because of its large signal significance. The optimized topological-selection cuts are listed in Tab. 1. Most selections are applied such that the two daughter tracks are likely to come from a common decay vertex with significant displacement from the collision point. Since the (anti)helium is much heavier than the decay daughter pion, the momentum and track direction of the (anti)helium are very close to those of the parent (anti)hypernuclei. Thus the (anti)helium DCA due to decay is too small to be clearly observed with STAR-TPC tracking resolution, and a lower limit on He $\chi^2_{primary}$ does not help to improve the signal. The very loose upper limit on He $\chi^2_{primary}$ is used here to reject background helium candidate tracks that are too far away from the collision point, for example, from pile-up events.

The invariant mass of a (anti)hypernucleus candidate is calculated as $\sqrt{(E_{He}+E_{\pi})^2-(\mathbf{p}_{He}+\mathbf{p}_{\pi})^2}$, where E and $\mathbf{p}$ are the energy and 3-dimensional momentum of the daughter particles.

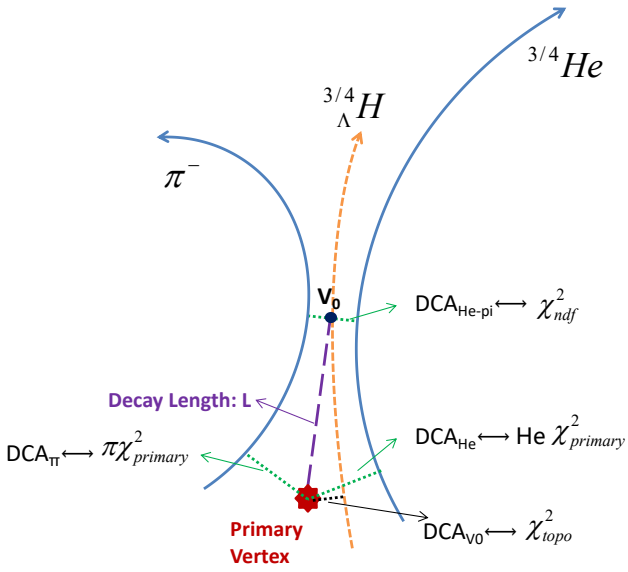

Figure 1: Illustration of the decay topology of a hypernucleus.

Background Subtraction. The invariant-mass distributions of the combinatorial backgrounds are reproduced with the rotation method. Before a helium track is paired with a pion track, its ϕ angle is rotated randomly in a range of $[30°, 330°]$. This procedure is repeated for 50 times to increase the statistics. Then the same topological-selection cuts as for signal-candidate selection are applied for the rotational background. They are then scaled so that the their integrals in two side-band regions

Table 1: Topological cuts for (anti)hypernucleus selection.

Particles	χ^2_{topo}	χ^2_{NDF}	$\pi\ \chi^2_{primary}$	He $\chi^2_{primary}$	L(cm)	L/dL
${}^{3}_{\Lambda}\mathrm{H}$, ${}^{4}_{\Lambda}\mathrm{H}$	< 2	< 5	> 10	< 2000	> 3.5	> 3.4
${}^{3}_{\bar{\Lambda}}\overline{\mathrm{H}}$, ${}^{4}_{\bar{\Lambda}}\overline{\mathrm{H}}$	< 3	< 5	> 10	< 2000	> 3.5	> 3.4

($2.941 \sim 2.987$ GeV/c^2 and $2.997 \sim 3.101$ GeV/c^2 for ${}^{3}_{\Lambda}\mathrm{H}$ and ${}^{3}_{\bar{\Lambda}}\overline{\mathrm{H}}$, $3.859 \sim 3.919$ GeV/c^2 and $3.925 \sim 4.019$ GeV/c^2 for ${}^{4}_{\Lambda}\mathrm{H}$ and ${}^{4}_{\bar{\Lambda}}\overline{\mathrm{H}}$) are equal to the integrals of the signal-candidate invariant-mass distributions in the same regions. The statistical uncertainties in the rotational background are obtained with a bootstrapping method. After that, the signal counts are extracted by subtracting the integrals of the scaled combinatorial-background distributions from the integrals of the signal-candidate distributions in the signal invariant-mass regions ($2.987 \sim 2.997$ GeV/c^2 for ${}^{3}_{\Lambda}\mathrm{H}$ and ${}^{3}_{\bar{\Lambda}}\overline{\mathrm{H}}$, $3.919 \sim 3.925$ GeV/c^2 for ${}^{4}_{\Lambda}\mathrm{H}$ and ${}^{4}_{\bar{\Lambda}}\overline{\mathrm{H}}$).

Significance Calculation. The signal significances in this analysis are obtained by calculating the likelihood ratios between the hypothesis of pure background and that of signal plus background. This is conducted both by counting the signal and background in a predefined signal invariant-mass region, and by fitting the candidate invariant-mass distribution without and with the signal. In the counting method, the significance is calculated by the asymptotic formula [9]

$$Z_{\mathrm{count}} = \sqrt{2\left[(N_{\mathrm{Sig}} + N_{\mathrm{Bg}})\ln\left(1 + \frac{N_{\mathrm{Sig}}}{N_{\mathrm{Bg}}}\right) - N_{\mathrm{Sig}}\right]}, \tag{1}$$

where the signal count N_{Sig} and background count N_{Bg} are obtained as described in the previous paragraph. In the fitting method, the candidate invariant-mass distribution is firstly fit by pure rotational background with a free scaling factor, then fit by rotational background plus a Gaussian-shaped signal. The Gaussian shape is due to the measured daughter-particle momentum resolution, which is propagated to the calculated invariant mass. All the Gaussian parameters are free in the fit. The likelihood ratios between the fits without and with the Gaussian-shaped signals are used to calculate the significances Z_{shape}.

Efficiency Correction. A correction is applied for the detector acceptance and reconstruction efficiency in the lifetime and yield ratio measurements. The acceptance and efficiency are obtained with an embedding Monte Carlo (MC) technique. (Anti)hypernuclei are simulated using a GEANT3 package, taking into account the geometry and materials of the STAR detectors [10]. The physical processes and the responses of the read-out electronics are simulated, and the final simulated data are embedded into real data events, which are sampled from different data-taking runs to have a good representation of the whole data set used in the analysis. The number of MC (anti)hypernuclei embedded is 5% of the multiplicity of the real-data events. Then the embedded events are processed through the same reconstruction procedures as real data. After that, the same track and topological requirements as for the real data are applied to the reconstructed MC (anti)hypernuclei. The final reconstruction efficiency ϵ is calculated as the ratio of the number of reconstructed MC (anti)hypernuclei to the number of input MC (anti)hypernuclei. This efficiency ϵ includes particle interaction with materials, the detector acceptance, tracking efficiency and selection efficiency. Since GEANT3 does not properly consider (anti)nucleus absorption by materials, we simulate the ^{3}He, $^3\overline{\text{He}}$, ^{4}He and $^4\overline{\text{He}}$ absorption using GEANT4, and further correct their track efficiency from the STAR official simulation. This correction is $<$3% for nuclei and $<$5% for antinuclei. The fraction of (anti)hypernuclei absorbed by the beam pipe (Be) and insulation gas (N_2) are estimated to be minimal and can be neglected.

The (anti)hypernucleus reconstruction efficiencies as a function of $L/(\beta\gamma)$ are shown in Fig. 2, which are used to correct the raw yields in different $L/(\beta\gamma)$ intervals before the exponential fits are conducted to extract the lifetimes.

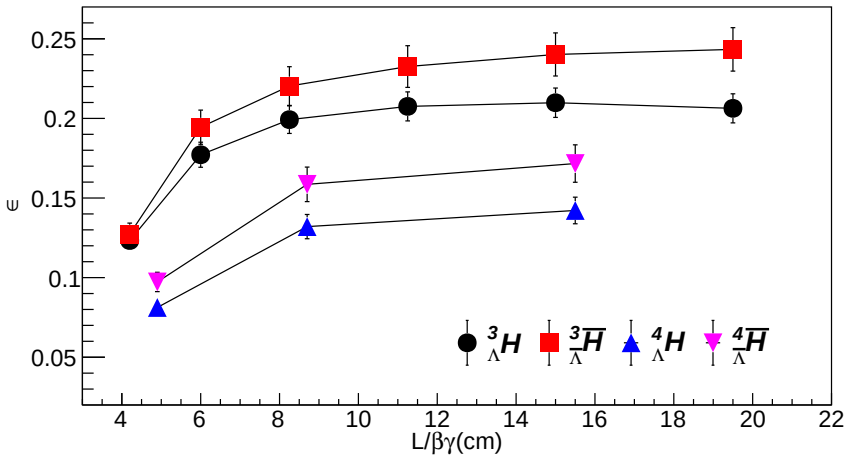

Figure 2: Reconstruction efficiency as a function of $L/(\beta\gamma)$ obtained from the embedding Monte Carlo technique. As shown in Tab. 1, hypernuclei have stricter topological cuts than antihypernuclei to suppress knock-out ^{3}He and ^{4}He, resulting in lower efficiencies.

(Anti)hypernuclei, Λ and $\bar{\Lambda}$ lifetime measurements. Figure 3 shows the invariant-mass distributions of $^{3}_{\Lambda}$H, $^{3}_{\bar{\Lambda}}\overline{\text{H}}$, $^{4}_{\Lambda}$H and $^{4}_{\bar{\Lambda}}\overline{\text{H}}$ candidates in different $L/(\beta\gamma)$ intervals, which are used to extract their lifetimes.

As an additional test of (anti)hypernucleus lifetime measurements, we have also measured the Λ and $\bar{\Lambda}$ lifetimes with the same method. 3.2 million Au+Au collision events at $\sqrt{s_{NN}} = 200$ GeV are used for these measurements. The topological cuts used to obtain the Λ signal are the same as those used in the (anti)hypernucleus analysis, except that an additional $V_0DCA < 0.1$ cm topological cut is added. V_0DCA is the distance-of-closest approach between the reconstructed mother-particle trajectory and the primary vertex. The V_0DCA cut suppresses contributions of Λ ($\bar{\Lambda}$) from Ξ ($\bar{\Xi}$) and Ω ($\bar{\Omega}$) decays, which make the measured lifetime longer. This is verified by

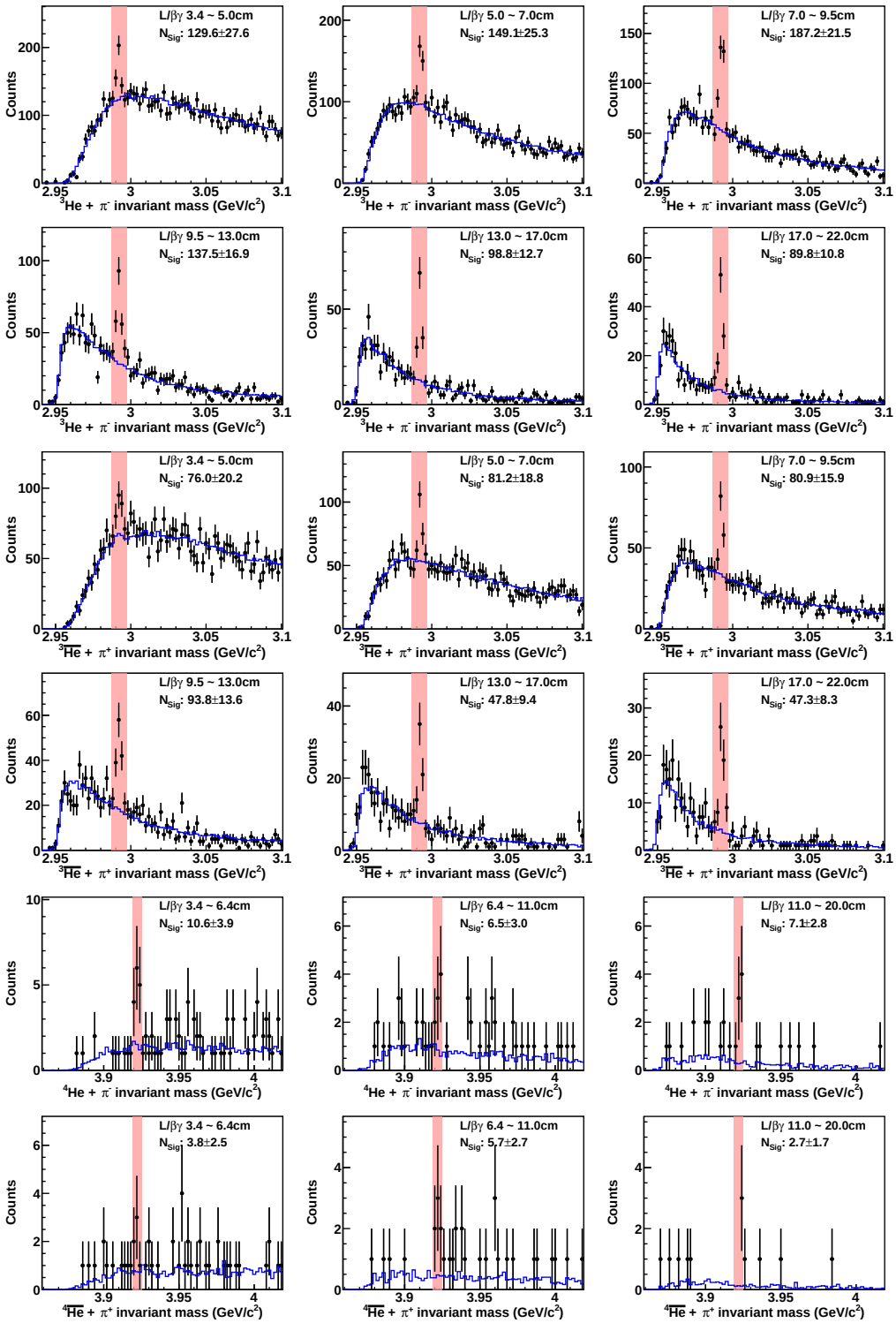

Figure 3: ${}^{3}_{\Lambda}\mathrm{H}$, ${}^{3}_{\Lambda}\overline{\mathrm{H}}$, ${}^{4}_{\Lambda}\mathrm{H}$ and ${}^{4}_{\Lambda}\overline{\mathrm{H}}$ candidate invariant-mass distributions in different $L/\beta\gamma$ intervals.

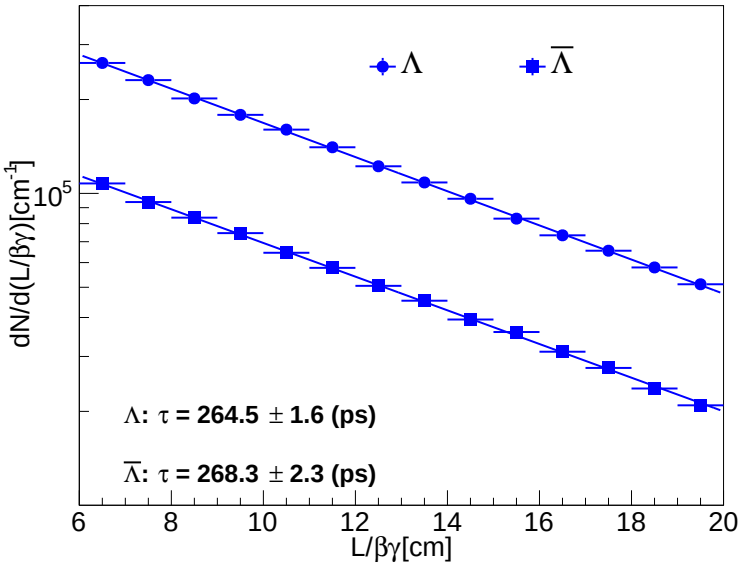

Figure 4: $dN/d(L/\beta\gamma)$ as a function of $L/\beta\gamma$ for Λ and $\bar{\Lambda}$, and exponential fits to obtain their lifetimes.

the fact that the measured Λ and $\bar{\Lambda}$ lifetimes increase as the allowed V_0DCA range is enlarged. Figure 4 shows the Λ and $\bar{\Lambda}$ $L/\beta\gamma$ distributions, and the exponential fits to obtain their lifetimes. Our measured lifetimes for Λ (264.5$\pm$1.6 ps) and $\bar{\Lambda}$ (268.3$\pm$2.3 ps) are consistent considering uncertainties, as expected by the CPT symmetry. However, they are slightly longer than the value from the Particle Data Group 263$\pm$2 ps [11]. This is expected because the V_0DCA cut can not exclude all Λ from Ξ and Ω decays. No particle yet discovered decays to ${}^{3}_{\Lambda}$H or ${}^{4}_{\Lambda}$H, so we do not consider the decay feed-down effect for (anti)hypernuclei lifetime measurements in this analysis.

Yield Measurements. The yields of all the studied particles in this work are measured in the phase space of $|y| < 0.7$ and $0.7 < p_{\rm T}/m < 1.5$ with only MB triggered events in order to avoid possible bias from the trigger selection. Thus the (anti)hypernucleus signal counts are less than those in

Fig. 3 in this paper. The signal and background counts that are used to extract (anti)hypernuclei yield ratios are listed in the Tab. 2.

Table 2: The signal and background counts in the measured phase space with MB triggered events.

Collision systems		${}^{3}_{\Lambda}\mathrm{H}$	${}^{3}_{\bar{\Lambda}}\overline{\mathrm{H}}$	${}^{4}_{\Lambda}\mathrm{H}$	${}^{4}_{\bar{\Lambda}}\overline{\mathrm{H}}$
Total	N_{Sig}	606 ± 42	317 ± 31	13.3 ± 4.1	8.3 ± 3.3
	N_{Bg}	1145 ± 6	605 ± 5	3.9 ± 0.3	2.7 ± 0.3
Au+Au, U+U	N_{Sig}	207 ± 27	89 ± 19	-	-
	N_{Bg}	517 ± 5	267 ± 4	-	-
Zr+Zr, Ru+Ru	N_{Sig}	400 ± 32	228 ± 24	-	-
	N_{Bg}	627 ± 4	339 ± 3	-	-

After $|n_{\sigma^{3}\mathrm{He}}| < 3$ and $1 < M^2/Z^2 < 3$ (GeV/c^2)^2 selections, the ^{3}He and $^3\overline{\mathrm{He}}$ candidates are counted with a $1/\epsilon$ weight to get the yield in the measured phase space.

For ${}^{3}_{\Lambda}\mathrm{H}$ and ${}^{3}_{\bar{\Lambda}}\overline{\mathrm{H}}$ yield measurements, invariant-mass distributions are obtained with a candidate-by-candidate $1/\epsilon$ weight. Then the signal yield is extracted by subtracting the combinatorial background, obtained by the rotation method, from the candidate invariant-mass distribution in the signal range.

For ^{4}He, $^4\overline{\mathrm{He}}$, ${}^{4}_{\Lambda}\mathrm{H}$ and ${}^{4}_{\bar{\Lambda}}\overline{\mathrm{H}}$, the statistics are too low to apply a candidate-by-candidate efficiency correction. We thus calculated the total raw yields in the whole selected p_{T} range and corrected it by the average efficiency. The average efficiency is obtained based on knowledge of the p_{T} spectra of $A = 3$ (anti)(hyper)nuclei. Firstly, the p_{T} spectra for ^{3}He, $^3\overline{\mathrm{He}}$, ${}^{3}_{\Lambda}\mathrm{H}$ and ${}^{3}_{\bar{\Lambda}}\overline{\mathrm{H}}$ are

obtained and fitted with Blast-Wave (BW) functions [12]

$$\frac{1}{2\pi p_T}\frac{d^2N}{dp_T dy} \propto \int_0^R r dr m_0 I_0\left(\frac{p_T \sinh\rho}{T}\right) K_1\left(\frac{m_T \cosh\rho}{T}\right), \quad (2)$$

as shown in Fig. 5. Here $\rho = \tanh^{-1}(\beta_s(r/R)^n)$ and $n = 1$. The fireball radius R is fixed at 10 fm. I_0 and K_1 are Bessel functions. m_0 is the particle mass, and $m_T = \sqrt{m_0^2 + p_T^2}$. β_s and T are free fitting parameters, representing the expansion velocity and temperature of the fireball. We then assume the BW functions for ^{4}He, $^4\overline{\text{He}}$, $^4_\Lambda$H and $^4_{\bar{\Lambda}}\overline{\text{H}}$ have the same β_s and T as for ^{3}He, $^3\overline{\text{He}}$, $^3_\Lambda$H and $^3_{\bar{\Lambda}}\overline{\text{H}}$, respectively, and the only difference in the BW functions are the particle masses. The efficiencies for ^{4}He, $^4\overline{\text{He}}$, $^4_\Lambda$H and $^4_{\bar{\Lambda}}\overline{\text{H}}$ in the whole measured p_T range are calculated as the average efficiency with the above BW-function weights. The measured raw yields of ^{4}He, $^4\overline{\text{He}}$, $^4_\Lambda$H and $^4_{\bar{\Lambda}}\overline{\text{H}}$ are then corrected with the average efficiencies to obtain the reported yields.

The yields of ^{3}He, $^3\overline{\text{He}}$, ^{4}He and $^4\overline{\text{He}}$ are also corrected for the contributions from the weak decays of $^3_\Lambda$H, $^3_{\bar{\Lambda}}\overline{\text{H}}$, $^4_\Lambda$H and $^4_{\bar{\Lambda}}\overline{\text{H}}$, whose fractions out of the total measured (anti)helium nuclei yields are listed in Tab. 3.

Table 3: Fraction of (anti)helium nuclei from the two-body weak decays of (anti)hypernuclei in different collision systems. The two-body decay branching fraction is 0.25 for $^3_\Lambda$H and $^3_{\bar{\Lambda}}\overline{\text{H}}$, 0.5 for $^4_\Lambda$H and $^4_{\bar{\Lambda}}\overline{\text{H}}$.

Collision systems	^{3}He	$^3\overline{\text{He}}$	^{4}He	$^4\overline{\text{He}}$
Total	(4.3±0.8)%	(4.9±1.1)%	(29±12)%	(42±21)%
Au+Au, U+U	(5.5±1.7)%	(6.2±2.5)%	-	-
Zr+Zr, Ru+Ru	(3.6±1.0)%	(4.0±1.5)%	-	-

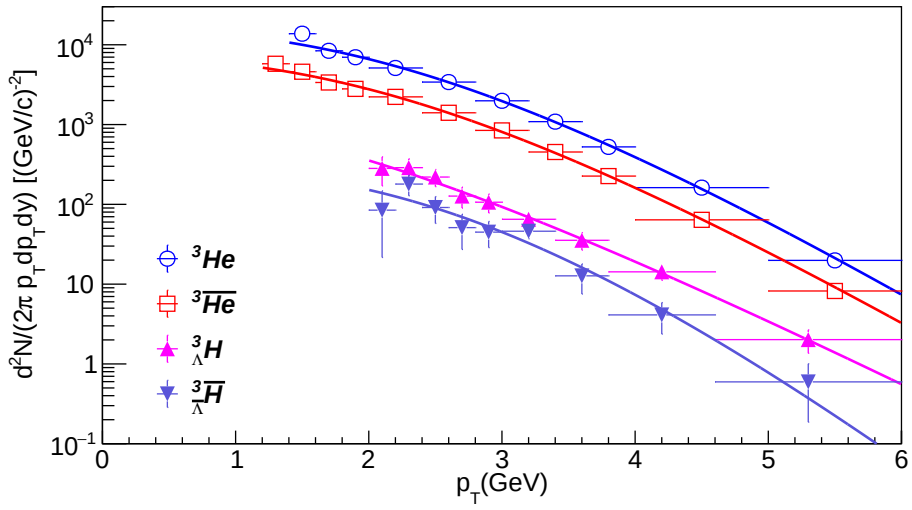

Figure 5: Efficiency corrected p_T spectra for ^{3}He, $^3\overline{\text{He}}$, $^3_\Lambda$H, and $^3_{\overline{\Lambda}}\overline{\text{H}}$. The spectra are in the phase space of $|y| < 0.7$ with only MB-triggered events. The spectra are not normalized by the number of events. The lines represent the BW-function fits.

While the measured particle ratios are consistent with previous measurements, we also note that the $^3_\Lambda\text{H}/^3\text{He}$ and $^3_{\overline{\Lambda}}\overline{\text{H}}/^3\overline{\text{He}}$ ratios in U+U and Au+Au collisions are lower than previous STAR results [13] by 2.8 and 1.9 σ, respectively. We have investigated possible sources of the differences. The previous analysis used a mixture of MB and central triggered events. The ratios are expected to be higher in central events [14,15]. The two analyses are also done in slightly different p_T ranges. These differences alone are not enough to explain the observed difference between the measured ratios at their face values. On the other hand, we note that the total uncertainties of those ratio measurements are large, of the order of $\pm 20 \sim 30\%$ themselves.

Systematic Uncertainties. Four major sources of systematic uncertainties are evaluated for the (anti)hypernucleus-lifetime measurements and the yield-ratio measurements: A. Systematic uncer-

tainties on track-reconstruction efficiency, evaluated by varying the minimal number of measured points on the tracks; B. Systematic uncertainties on (anti)hypernucleus reconstruction efficiency due to topological selections, evaluated by varying the topological-selection viarables; C. Systematic uncertainties on (anti)hypernucleus signal-yield extraction from the invariant-mass spectra, evaluated by enlarging the invariant-mass ranges for signal-yield integration; and systematic uncertainties from the p_T-spectrum shapes, evaluated by narrowing the p_T-spectrum fit ranges; D. Systematic uncertainties on the (anti)helium yields, evaluated by varying the minimal number of measured points for $\langle dE/dx \rangle$ calculation and the cut on the helium-track DCA to primary vertex. The total systematic uncertainty is calculated as the quadratic sum of the four contributions above. The systematic uncertainty contributions from different sources for lifetime and yield-ratio measurements are summarized in Tab. 4, Tab. 5 and Tab. 6. When calculating the yield ratios, lifetimes and lifetime differences, the correlations of systematic uncertainties from the same sources have been considered. Thus part of systematic uncertainties will be canceled.

Table 4: Systematic uncertainties on (anti)hypernucleus lifetimes.

Sources	$\tau(^{3}_{\Lambda}\mathrm{H})$	$\tau(^{3}_{\bar{\Lambda}}\overline{\mathrm{H}})$	$\tau(^{4}_{\Lambda}\mathrm{H})$	$\tau(^{4}_{\bar{\Lambda}}\overline{\mathrm{H}})$
Track reconstruction	2.8%	8.9%	15.5%	16.8%
Topological selection	4.5%	7.3%	11.9%	10.5%
Signal extraction & p_T shape	0.4%	0.5%	2.4%	3.8%
Total	5.4%	11.6%	19.7%	20.1%

Table 5: Systematic uncertainties on yield ratios in all measured collision systems.

Sources	$\frac{^3\overline{\mathrm{He}}}{^3\mathrm{He}}$	$\frac{^4\overline{\mathrm{He}}}{^4\mathrm{He}}$	$\frac{^3_{\Lambda}\overline{\mathrm{H}}}{^3_{\Lambda}\mathrm{H}}$	$\frac{^4_{\Lambda}\overline{\mathrm{H}}}{^4_{\Lambda}\mathrm{H}}$	$\frac{^3_{\Lambda}\mathrm{H}}{^3\mathrm{He}}$	$\frac{^4_{\Lambda}\mathrm{H}}{^4\mathrm{He}}$	$\frac{^3_{\Lambda}\overline{\mathrm{H}}}{^3\overline{\mathrm{He}}}$	$\frac{^4_{\Lambda}\overline{\mathrm{H}}}{^4\overline{\mathrm{He}}}$
Track reconstruction	0.6%	0.6%	12.6%	12.6%	5.8%	5.8%	10.8%	10.8%
Topological selection	0.6%	0.6%	11.4%	11.4%	3.8%	3.8%	13.7%	13.7%
Signal extraction & p_T shape	0.1%	22.2%	1.9%	46.3%	6.0%	20.4%	8.2%	49.9%
(Anti)helium yields	0.3%	0.3%	-	-	3.4%	3.4%	3.2%	3.2%
Total	0.9%	22.2%	17.1%	49.3%	9.8%	21.8%	19.5%	52.9%

Table 6: Systematic uncertainties on yield ratios in big and small collision systems.

	Au+Au, U+U		Zr+Zr, Ru+Ru	
Sources	$\frac{^3_{\Lambda}\mathrm{H}}{^3\mathrm{He}}$	$\frac{^3_{\Lambda}\overline{\mathrm{H}}}{^3\overline{\mathrm{He}}}$	$\frac{^3_{\Lambda}\mathrm{H}}{^3\mathrm{He}}$	$\frac{^3_{\Lambda}\overline{\mathrm{H}}}{^3\overline{\mathrm{He}}}$
Track reconstruction	8.1%	27.0%	3.6%	4.9%
Topological selection	7.0%	28.9%	3.7%	7.9%
Signal extraction & p_T shape	15.1%	18.3%	3.0%	0.6%
(Anti)helium yields	4.2%	3.5%	3.8%	1.9%
Total	19.0%	43.7%	7.1%	9.5%

Reference

1. Llope, W. *et al.* The TOFp/pVPD Time-of-flight System for STAR. *Nuclear Instruments and Methods A* **522**, 252–273 (2004).

2. Adler, C. *et al.* The RHIC Zero Degree Calorimeters. *Nuclear Instruments and Methods A* **470**, 488–499 (2001).

3. Llope, W. J. and STAR collaboration et al. Multigap RPCs in the STAR Experiment at RHIC. *Nuclear Instruments and Methods A* **661**, S110–S113 (2012).

4. Beddo, M. *et al.* The STAR Barrel Electromagnetic Calorimeter. *Nuclear Instruments and Methods A* **499**, 725–739 (2003). The Relativistic Heavy Ion Collider Project: RHIC and its Detectors.

5. Kisel, I., Kulakov, I. & Zyzak, M. Standalone First Level Event Selection Package for the CBM Experiment. In *Proceedings, 18th Real-Time Conference (RT2012) : Berkley, USA, June 11-15, 2012* (2012).

6. Zyzak, M. *Online Selection of Short-lived Particles on Many-core Computer Architectures in the CBM Experiment at FAIR*. Ph.D. thesis, Johann Wolfgang Goethe-Universität (2016).

7. Ju, X.-Y. *et al.* Applying the Kalman filter particle method to strange and open charm hadron reconstruction in the STAR experiment. *Nucl. Sci. Tech.* **34**, 158 (2023).

8. Ablyazimov, T. O., Zyzak, M. V., Ivanov, V. V. & Kisel, P. I. Kalman filter-based fast track reconstruction for charged particles in a Compressed Baryonic Matter experiment using parallel

computing on a multicore server at the Laboratory of Information Technologies, Joint Institute for Nuclear Research. *Phys. Part. Nucl. Lett.* **12**, 423–427 (2015).

9. Cowan, G., Cranmer, K., Gross, E. & Vitells, O. Asymptotic formulae for likelihood-based tests of new physics. *Eur. Phys. J. C* **71**, 1554 (2011). [Erratum: Eur.Phys.J.C 73, 2501 (2013)], 1007.1727.

10. Fine, V. & Nevski, P. OO Model of STAR Detector for Simulation, Visualisation and Reconstruction. In *11th International Conference on Computing in High-Energy and Nuclear Physics*, 143–146 (2000).

11. Group, P. D. *et al.* Review of Particle Physics. *Progress of Theoretical and Experimental Physics* **2022**, 083C01 (2022).

12. Schnedermann, E., Sollfrank, J. & Heinz, U. W. Thermal Phenomenology of Hadrons from 200-A/GeV S+S Collisions. *Phys. Rev. C* **48**, 2462–2475 (1993). nucl-th/9307020.

13. Abelev, B. I. *et al.* Observation of an Antimatter Hypernucleus. *Science* **328**, 58–62 (2010). 1003.2030.

14. Sun, K.-J., Ko, C. M. & Dönigus, B. Suppression of light nuclei production in collisions of small systems at the Large Hadron Collider. *Phys. Lett. B* **792**, 132–137 (2019). 1812.05175.

15. Bellini, F. & Kalweit, A. P. Testing production scenarios for (anti-)(hyper-)nuclei and exotica at energies available at the CERN Large Hadron Collider. *Phys. Rev. C* **99**, 054905 (2019). 1807.05894.